Title: Parametric inverse impulse response based on reduced
order modeling and randomized excitations

SANTIAGO MONTAGUD

Univ. Bordeaux, ESTIA INSTITUTE OF TECHNOLOGY, I2M
UMR 5295, F-64210 Bidart, France
santiago.montagud-perez-de-lis@u-bordeaux.fr

JOSÉ VICENTE AGUADO

ICI, Ecole Centrale de Nantes
1 rue de la Noe, BP 92101, F-44321 Nantes cedex 3, France
jose.aguado-lopez@ec-nantes.fr

FRANCISCO CHINESTA

Arts et Métiers ParisTech, ESI Chair
UMR 8006 CNRS-ENSAM, F-75013 Paris, France
francisco.chinesta@ensam.eu

PIERRE JOYOT

Univ. Bordeaux, ESTIA INSTITUTE OF TECHNOLOGY, I2M
UMR 5295, F-64210 Bidart, France
p.joyot@estia.fr

1

Abstract

This paper is concerned with the computation of the inverse impulse response of a parametrized structural dynamics problem using reduced-order modeling and randomized excitations. A two-stages approach is proposed, involving the solution of both direct and inverse problems. In the first stage, the parametrized structural dynamics problem is formulated in the frequency domain, and solved using a reduced-order modeling approach. As a result, the parametric transfer function of the structure is obtained, and then readily transformed into a parametric direct impulse response (DIR). In the second stage, the parametric inverse impulse response (IIR) is computed. We use randomized excitations to generate synthetic samples inexpensively from the parametric DIR. Based on these, the parametric IIR is computed by minimizing the mean square error between the estimate and the samples. Most importantly, we show that the randomized excitations can be generated by sampling the frequency domain only. Hence, the parametric domain does not need to be sampled, which makes the computation of the parametric IIR very efficient.

1   Introduction

Real-time reconstruction of both dynamic forces acting on a structure and the system state (e.g. structure displacements) is of great importance in many engineering applications. While the system state can often be measured at least at specific locations, dynamic forces acting on a structure are generally unknown. Extensive research has been done over the past decades in order to estimate the time history of dynamic forces from indirect measures [42, 43, 44, 45, 46, 47, 48, 49].

The dynamic forces recovery problem can be seen as a particular instance of general inverse problems. Literature in this area is vast and covers almost every area of science and engineering. However, in next lines we give a general overview on the main approaches that have been proposed in the literature to address the ill-posedness of the dynamic forces recovery problem. In the framework of linear time-invariant (LTI) systems, it is well known that the impulse response fully captures the system behavior. In particular, the system response can be computed from the convolution of the impulse response and the input signal, that is the force. In this framework, deconvolution is used to reverse the effects of convolution on the system's response. A naive deconvolution approach based on direct inversion of the impulse response would fail because of the drastic amplification of the noise inherent to both measures and computations. There is a vast literature aiming at addressing the noise amplification issue in deconvolution [35, 18, 19].

Regularization methods are based on a functional description of the signal (force, system response) [18, 7]. In particular, we require the *deconvolved* signal to belong to a certain functional space and to minimize a certain error measure. Several regularization techniques have been proposed over the years, including Tikhonov regularization [35], which can be used to constrain the solution to

the space of square-integrable functions, for instance. In other fields, such as image processing, more sophisticated functional spaces may be preferable [6]. Finally, iterative regularization methods have also been proposed in order to address large-scale systems, such as Landweber iteration [27]. Since applications of signal and image processing are virtually unlimited, many field-specific deconvolution methods have been proposed in areas such as radioastronomy [25], optics [37] or geophysics [34], just to cite few examples.

The inverse problem can also be posed into a statistical framework, which uses a statistical description of the signals and certain assumptions on the nature of the noise. This approach is particularly fruitful in the field of signal processing. The main advantage is that filtering theory for LTI systems, i.e. Wiener filtering and deconvolution, was extended to general dynamical systems by Kalman filtering [24], and also nonlinear dynamical systems (extended Kalman filter) [16]. Finally, Bayesian filtering provides an even more general framework which reduces to the Kalman filter if variables are normally distributed and transitions are linear. Examples using statistical framework can be found in [22].

Besides to the ill-posedness of the dynamic forces recovery problem, at least two other important challenges can be identified in the literature. The first one concerns the trade-off between model accuracy and real-time performance. Many practical applications impose a real-time performance constraint which is not always easy to meet, especially when simple dynamical models, such as concentrated parameters models, cannot be assumed. Hybrid laboratories [1, 23] or soft robotics [13, 33] are two examples of new industrial applications which require continuum mechanics modeling in order to describe both deformation and forces properly. They usually result in large-scale computer models which are most likely incompatible with the real-time constraint. The second challenge concerns model adaptivity to structural alterations and/or uncertainties. Structures are prone to evolve and deteriorate over the time, making it very difficult to assess the validity of structural models beforehand.

Reduced-order modeling (ROM) methods [8, 29, 14] constitute an appealing alternative in order to address both previous challenges. ROM methods are well-known for providing a scientific and mathematical basis for fast simulation, sometimes even in real-time, of engineered systems. The basic idea is to exploit the fact that the solution of many models can be approximated very efficiently provided that a suitable representation basis is chosen. The two principal families of ROM methods, *a priori* and *a posteriori* methods, differ essentially on how they build such appropriate representation basis. In this paper, we are only concerned with the *a-priori* ROM methods, and more specifically, with the Proper Generalized Decomposition (PGD) [10][15].

In this work, we propose a two-stages approach involving the solution of both parametric direct and inverse problems, using PGD and randomized excitations. The proposed approach is only concerned with the forced response of LTI systems. In the first stage, we rely on parametric direct impulse responses (DIR), already introduced in [2] in the context of thermal problems, and applied to structural dynamics in [17, 28]. The computation of the parametric DIR in-

3

volves a frequency-domain formulation of the structural dynamics problem for reasons that will be made clear in Section 2. The key aspect of the parametric DIR is that it does not only encode the system response, but also captures the system behavior in a wide range of scenarios thanks to its parametric nature. Specifically, if parameters represent structural alterations and/or uncertainties, the parametric DIR can account for these changes and still be able to predict the system response. In addition, the parametric DIR offers a simple procedure to obtain a real-time feedback of the displacements via its convolution with the excitation force.

In the second stage, we use randomized excitations to generate synthetic samples inexpensively from the parametric DIR. Then, the parametric inverse impulse response (IIR) is computed by minimizing the mean square error between the estimate and the samples using PGD. Most importantly, we show that the randomized excitations can be generated by sampling the frequency domain only. Hence, the parametric domain does not need to be sampled, which makes the computation of the parametric IIR very efficient. In summary, the objective of this work is to compute a parametric inverse impulse response which is able to compute the excitation force by reversing the effects of the structure on the measured displacement, and that is able to do so in a wide range of scenarios thanks to its parametric nature. Figure 1 show a general picture of the method.

The rest of the paper is organized as follows. Section 2 presents the model problem being considered in this paper, first in the time domain, and then we move to the frequency domain. In Section 2.3 we give a brief sketch on the computation of the parametric DIR using the PGD method. We then show how to use the parametric DIR for real-time monitoring of displacements under arbitrary force. Section 3 is concerned with the computation of the parametric IIR. We first give in Section 3.1 a brief outline of the proposed strategy in a non-parametric framework. Then, in Section 3.2 we show how to generate synthetic samples for the parametric DIR, which are then used to set up a regularized minimization problem to compute the parametric IIR. We give the details of the PGD computation of the parametric IIR in Section 3.2.2, which can be completed with details in Appendix A. Section 4 is concerned with some numerical examples that serve to test the performance of the proposed approach. Finally, conclusions are drawn in Section 5.

2   Monitoring displacement

In this section we review the formulation of the direct problem, that is, computing displacements from known forces, and show how to compute the parametric DIR. In order to compute the impulse response, the problem is first formulated in the frequency domain, and then the solution transformed back to the time domain. Therefore, we start with the model problem in the time domain and then we move to a frequency-domain formulation. Finally, we show how the parametric DIR can be used for real-time monitoring of displacements. This constitutes the first stage of the approach presented in this paper.

2.1 Model problem in the time domain

For the purposes of this paper, we consider a linear visco-elastic body that occupies an open bounded domain $\Omega \subset \mathbb{R}^{d \leq 3}$. Its boundary, $\partial\Omega$, is partitioned into two disjoint parts, Neumann Γ_N and Dirichlet Γ_D frontiers, such that $\partial\Omega = \bar{\Gamma}_N \cup \bar{\Gamma}_D$. Under the assumption of small perturbations, the evolution of displacements $\mathbf{u}(t)$ in the time interval of interest, $t \in I_t = [0, T_{\text{final}}]$, is governed by the elastodynamic equation of motion:

$$\begin{cases} \rho\ddot{\mathbf{u}} - \boldsymbol{\nabla} \cdot \boldsymbol{\sigma} = \mathbf{0} & \text{in} \quad \Omega \times I_t, \\ \boldsymbol{\sigma} \cdot \mathbf{n} = \mathbf{t} & \text{on} \quad \Gamma_N \times I_t, \\ \mathbf{u} = \mathbf{0} & \text{on} \quad \Gamma_D \times I_t, \end{cases} \tag{1}$$

where ρ is the mass density, $\boldsymbol{\sigma}$ is the stress and $\mathbf{n}$ is the outward unit normal to $\partial\Omega$. On the other hand, $\mathbf{t}$ stand for the surface traction. Appropriate initial conditions for $\mathbf{u}$ and $\dot{\mathbf{u}}$ at $\Omega \times \{0\}$ must also be provided. Eq. (1) is closed with the constitutive law, the Kelvin-Voigt linear visco-elastic model,

$$\boldsymbol{\sigma} = \mathbf{D} : (\boldsymbol{\varepsilon} + \tau\dot{\boldsymbol{\varepsilon}}), \tag{2}$$

where $\mathbf{D}$ is the fourth-order Hooke elasticity tensor and τ is a characteristic time related to the viscous behavior. According to the small perturbations hypothesis, $\boldsymbol{\varepsilon} = \dfrac{1}{2}\left(\boldsymbol{\nabla}\mathbf{u} + \boldsymbol{\nabla}^t\mathbf{u}\right)$.

Upon discretization, e.g. using the finite element method [5], we arrive to the matrix differential equations of motion,

$$\mathbf{M}\ddot{\mathbf{u}}(t) + \mathbf{C}\dot{\mathbf{u}}(t) + \mathbf{K}\mathbf{u}(t) = \mathbf{f}(t), \tag{3}$$

where $\mathbf{M}, \mathbf{C}, \mathbf{K} \in \mathbb{R}^{N \times N}$ are the mass, damping and stiffness matrices, respectively, $\mathbf{f}(t) \in \mathbb{R}^N$ is the generalized force vector and $\mathbf{u}(t) \in \mathbb{R}^N$ is from now on the generalized displacement vector. Since structural dynamics have been studied in many scientific articles and textbooks [4, 21, 38], we do not provide here an exhaustive literature review.

Many methods have been proposed over the time in order to solve Eq. (3), including time-integration schemes [38], modal methods [12] and frequency-domain methods based on harmonic analysis [30]. In spite of their wide applicability, these methods are not always suitable for real-time computation. Besides, they are not designed to accommodate structural alterations or uncertainty, at least in combination with the real-time constraint. Time integration schemes, for instance, could not be fast enough in stochastic frameworks, where calibration and active control must coexist. Moreover, modal methods cannot deal easily with structural changes and uncertainties, because in principle, the modal basis would have to be computed each time a change in the structure takes place [36]. We recommend the interested reader the works [40, 41] for more information about efficient computation of the modes under structural modifications.

2.2 Forced response via frequency domain formulation

Frequency-domain representations are a powerful approach to study the response of the structure when initial conditions can be neglected, that is, we are only concerned with the forced response. This framework, which was integrated into the finite element (FE) framework from the very beginning, still is extensively used today. Since it is well described in many textbooks [11], it is not our aim to provide a detailed literature review here.

Consider that our dynamic system is submitted to some dynamic action represented by the generalized force vector, $\mathbf{f}(t)$. Under rather weak conditions, it is possible to obtain a *frequency representation*, $\mathbf{f}(\omega)$, of the generalized force vector via the direct Fourier Transform. And *vice versa*, from the frequency representation it is possible to recover the *time representation* of the generalized force vector via the inverse Fourier Transform. The pair of direct/inverse transforms is defined as follows:

$$\mathbf{f}(\omega) = \int_{-\infty}^{+\infty} \mathbf{f}(t) \exp\left(-\mathrm{i}\omega t\right) dt \quad \text{and} \quad \mathbf{f}(t) = \frac{1}{2\pi} \int_{-\infty}^{+\infty} \mathbf{f}(\omega) \exp\left(\mathrm{i}\omega t\right) d\omega.$$

No distinct notation is used for time-domain or frequency-domain representations for the sake of simplicity. Analogously, we may also consider the frequency representation of the generalized displacement vector, $\mathbf{u}(\omega)$, that may be computed from

$$\left(-\omega^2 \mathbf{M} + \mathrm{i}\omega \mathbf{C} + \mathbf{K}\right) \mathbf{u}(\omega) = \mathbf{f}(\omega). \tag{4}$$

Notice that Eq. (4) is obtained by taking the Fourier transform over Eq. (3). It can be seen that the dynamic response depends parametrically on ω. This parametric dependence is intrinsic to harmonic analysis and renders it very unattractive when compared to modal analysis or even direct integration. In practice, harmonic analysis is only used to compute the response against rather simple (with few frequencies) periodic forcing terms. If arbitrary (non-periodic) forcing terms are of interest, in principle one has to deal with a continuous frequency spectrum.

2.3 Computing the direct impulse response with PGD

In this section, we use the PGD method in order to deal with the parametric nature of the frequency-domain formulation, Eq. (4). Specifically, we shall compute a parametric solution in terms of the frequency. Then, by coming back to the time domain, we obtain the direct impulse response. If extra parameters (other than frequency) are considered in the PGD formulation, we can obtain a parametric DIR.

Space-frequency separated representations have also been considered in [31, 32] for the so-called variational theory of complex rays. Obviously, there have been many attempts considering such descriptions within the model reduction framework; the interested reader can refer to [20, 39] and the references therein.

Let us assume that the excitation can be expressed as a combination of harmonics:

$$\mathbf{f}(t) = \mathbf{f}_s p(t), \tag{5}$$

where $\mathbf{f}_s$ is the vector that collects the space distribution of the excitation and $p(t)$ is a function that modulates the excitation in time. Following classic analysis of LTI systems, the transfer function of the system, denoted by $\mathbf{h}(\omega) \in \mathbb{R}^N$, can be computed as the solution against the impulse. That is, we consider $p(t) \equiv \delta(t)$, where $\delta(t)$ stands for the Dirac's delta distribution. Recalling that $\mathbf{f}(\omega) = \mathbf{f}_s p(\omega)$ and $p(\omega) = \delta(\omega) = 1$, we arrive to:

$$\left(-\omega^2 \mathbf{M} + i\omega \mathbf{C} + \mathbf{K}\right) \mathbf{h}(\omega) = \mathbf{f}_s. \tag{6}$$

Note that, if we were able to solve Eq. (6) for every frequency, we would dispose of the *transfer function* of the system, which implies that the system response under arbitrary $p(t)$ could be obtained readily. Therefore, the idea is to use a ROM approach, based on the PGD method, to compute $\mathbf{h}(\omega)$ efficiently for every frequency in the interval of interest, i.e. $\omega \in I_\omega = [\omega^-, \omega^+]$.

PGD devises an *offline-online* strategy to alleviate the computational burden and reach real-time performance. In the offline stage, PGD encodes the system response for a wide variety of scenarios, described by the parameters. For the time being, we are only considering the frequency as a parameter, but as it will be shown later, several parameters could be considered. This leads naturally to a multi-dimensional problem which has to be addressed carefully in order to avoid the so-called *curse of dimensionality* [50]. PGD makes use of separated-variables representations, that is, the solution is sought as a sum of function products, where each function depends on one parameter. The key point of the PGD algorithm is to split the complexity of multi-dimensional problems into lower-dimensional ones, much less complex to solve. Specifically, the transfer function is sought using the following space-frequency separated representation:

$$\mathbf{h}(\omega) = \sum_{i=1}^n \mathbf{X}_i \, W_i(\omega), \tag{7}$$

where $\mathbf{X}_i$ collects the nodal generalized *space modes* and $W_i(\omega)$ denotes the *frequency modes* of the solution. Both are a priori unknown and must be determined by the algorithm. PGD builds Eq. (7) using a greedy enrichment that adds one term at a time. Each term is computed using an alternating direction method. The enrichment process is stopped using appropriate error estimation. More detailed information about the procedure can be found in [9].

As noted previously, space-frequency separated representations can be generalized by considering extra parameters other than frequency. We can take advantage of this feature in order to deal with structural alterations and/or uncertainties. For illustrative purposes, let us assume that the elastic behavior of the structure is not fully characterized, e.g. we do not have a precise knowledge of one of the Young's modulus. Instead, we may have access to a probability density function of the Young's modulus. Parametric solutions offer a simple

manner to account for that uncertainty, which consists in computing a parametric transfer function in terms not only of the frequency, but also the Young's modulus. Let us assume Young's modulus $E \in I_E = [E^-, E^+]$. PGD allows computing a separated solution in the form:

$$\mathbf{h}(\omega, E) = \sum_{i=1}^{n} \mathbf{X}_i \, W_i(\omega) \, \mathcal{E}_i(E), \tag{8}$$

where $\mathbf{X}_i$ collects the nodal generalized space modes, W_i is a frequency mode and $\mathcal{E}_i$ is a Young's modulus mode.

Note that, in the online stage, the parametric transfer function defined in Eq. (8) can be accessed in real-time for any parameter combination by performing no more than look-up table operations.

Remark (Alternative separated formats). *Although basis vectors $\mathbf{X}_i$ and functions $W_i(\omega)$ are denoted exactly the same in Eq. (7) and Eq. (8) for notational simplicity, we are not implying that both bases are the same. They will be different in general, and neither $\mathbf{X}_i$ nor $W_i(\omega)$ in Eq. (7) are reused in Eq. (8) (although it is theoretically possible). The number of basis terms, denoted by n both in Eq. (7) and Eq. (8), is different as well. Eq. (8) uses a canonical format, which is at the base of the PGD method used here [9]. However, other formats are possible and, in some cases, can be more convenient. The interested reader can refer to [51] for an introductory review on the topic of tensor formats and their decomposition.*

2.4   Real-time monitoring of displacements

Once the parametric transfer function, Eq. (8), is available, we can apply simple LTI systems theory in order to recover the parametric DIR. Since both Fourier direct and inverse transforms are linear applications, the parametric impulse response can be written as follows:

$$\mathbf{h}(t, E) = \mathcal{F}^{-1} \left[\mathbf{h}(\omega, E) \right] = \sum_{i=1}^{n} \mathbf{X}_i \, W_i(t) \, \mathcal{E}_i(E),$$

where $W_i(t) = \mathcal{F}^{-1}[W_i(\omega)]$ represents the inverse Fourier transform of frequency-domain modes in Eq. (8). Note that the inverse Fourier transform is applied only on frequency modes, which renders the operation extremely efficient.

Now the parametric DIR can be used to compute the response of the structure under an arbitrary excitation $p(t)$:

$$\mathbf{u}(t, E) = \int_0^t p(t - \tau) \, \mathbf{h}(\tau, E) \, \mathrm{d}\tau, \tag{9}$$

where $\mathbf{u}(t, E)$ is a parametric solution that collects the time evolution of the nodal displacements, for all $E \in I_E$. Note that the convolution is done between

$p(t)$ and each component of the parametric impulse response $\mathbf{h}(t, E)$:

$$\mathbf{u} = \begin{bmatrix} u_1(t, E) = \int_0^t p(t - \tau) h_1(\tau, E) \, d\tau \\ \vdots \\ u_N(t, E) = \int_0^t p(t - \tau) h_N(\tau, E) \, d\tau \end{bmatrix}.$$

It is worth to highlight that Eq. (9) allows computing displacements only at those degrees of freedom of interest (e.g. those where measures are actually done), and consequently an important computational cost can be saved. Thanks to linearity, convolution can be applied only to time-dependent modes, $W_i(t)$. We can therefore define:

$$\Upsilon_i(t) = \int_0^t p(t - \tau) \, W_i(\tau) \, d\tau,$$

and the parametric displacements are written as follows:

$$\mathbf{u}(t, E) = \sum_{i=1}^n \mathbf{X}_i \, \Upsilon_i(t) \, \mathcal{E}_i(E). \tag{10}$$

Therefore, displacements can be readily evaluated from the parametric DIR, under arbitrary force excitations and for a variety of Young's modulus values. Eventually, this feature could be used to reverse-engineer the Young's modulus based on simulation predictions, or to propagate uncertainty if a probability density function on the Young's modulus is available. However, in this paper we will use randomized excitations to generate synthetic samples inexpensively from the parametric DIR.

3 Monitoring force via parametric inverse impulse response

While displacements can often be measured at least at specific locations, dynamic forces acting on a structure are generally unknown. Real-time estimation of dynamic forces is of great importance in many engineering applications. For instance, in hybrid laboratories [1, 23] combine experimentation in the part of the system where complex (i.e. not well-established) physics happen, and simulation where models can be trusted. Both experiment and simulation communicate via some actuator. Real-time feedback from the simulation is therefore critical.

However, the force recovery problem is not straightforward as Eq. (3) may not have unique solution for an unknown force. In this section, we address the force recovery problem in a parametric framework. Starting with the parametric DIR computed in Section 2, we compute a parametric inverse impulse response using randomized excitations and a PGD formulation.

3.1 Outline of the proposed strategy

The concept of inverse impulse response (IIR) is at the center of the proposed strategy. Suppose displacement is measured at node j, with $1 \leq j \leq N$; then, the IIR associated to that node, $g_j(t)$, allows to reverse the effects of the structure on $u_j(t)$ and delivers the excitation force $p(t)$:

$$p(t) = u_j(t) * g_j(t) \equiv \int_0^t u_j(t - \tau) \, g_j(\tau) \, d\tau, \tag{11}$$

where "$*$" stands for the convolution operation. Note that $p(t)$ is the force amplitude modulation, as defined in Eq. (5). Parametric dependency has been ignored in Eq. (11) for the sake of notational simplicity. Moreover, note that Eq. (11) makes the (physically reasonable) hypothesis that $h_j^{-1}(\omega)$ is well defined for all ω in the range of interest [52].

Computing the IIR can be seen as a deconvolution problem. As reviewed in Section 1, one of the main approaches to address the ill-posedness of the inverse problems is regularization [35]. This approach makes use of a functional description of the signal, and in particular, requires the deconvolved signal to belong to a certain functional space and to minimize a certain error measure. Although other options are possible, here we follow a regularization approach based on the use of training samples.

Suppose we are given a set of force samples and its corresponding displacements, denoted by $\{p_\ell(t), \mathbf{u}_\ell(t)\}_{\ell=1}^{n_{\text{train}}}$, respectively. Note that, in particular, displacements could be computed from the direct impulse response inexpensively as $\mathbf{u}_\ell(t) = \mathbf{h}(t) * p_\ell(t)$. Then, in order to compute the IIR we consider a regularized approach that seeks to minimize the mean square error between the estimate and the samples:

$$\sum_{\ell=1}^{n_{\text{train}}} \|u_{\ell j}(t) * g_j(t) - p_\ell(t)\|^2 + \lambda \|S(g_j(t))\|^2 \quad \text{for} \quad 1 \leq j \leq N, \tag{12}$$

where $\|\bullet\|$ denotes the standard L^2 norm over I_t, the time interval of interest; $u_{\ell j}(t)$ denotes the j-th entry of $\mathbf{u}_\ell(t)$; λ is the regularization parameter; and $S(\bullet)$ is some linear operator in order to enforce the desired properties to the solution. Note that the problem defined in Eq. (12) is *uncoupled* with respect to the degree of freedom j; that is, $g_j(t)$ can be computed independently from $g_k(t)$, with $k \neq j$.

By discretizing the time domain, and taking into account that convolution is a linear operator, Eq. (12) can be written in matrix form as follows:

$$\sum_{\ell=1}^{n_{\text{train}}} \|\mathbf{U}_{\ell j}\mathbf{g}_j - \mathbf{p}_\ell\|_2^2 + \lambda \|\mathbf{S}\mathbf{g}_j\|_2^2, \tag{13}$$

where $\mathbf{U}_{\ell j}$ represents the discrete convolution operator associated to $u_{\ell j}(t)$. On the other hand, $\mathbf{S}$ is the equivalent discrete of $S(\bullet)$, usually equal to the identity

matrix if we seek the solution with minimum norm, or a Laplace operator, if we want to enforce smoothness of the solution. Eq. (13) yields the solution:

$$\mathbf{g}_j = \left(\sum_{\ell=1}^{n_{\text{train}}} \mathbf{U}_{\ell j}^T \mathbf{U}_{\ell j} + \lambda \mathbf{S}^T \mathbf{S} \right)^{-1} \left(\sum_{\ell=1}^{n_{\text{train}}} \mathbf{U}_{\ell j}^T \mathbf{p}_\ell \right). \tag{14}$$

3.2 Parametric inverse impulse response

In Section 3.1 parametric dependencies have been omitted for the sake of simplicity. Now we seek a parametric inverse impulse response in the following separated-variables format,

$$\mathbf{g}(t, E) = \sum_{l=1}^{\bar{n}} \bar{\mathbf{X}}_l \, \bar{W}_l(t) \, \bar{\mathcal{E}}_l(E), \tag{15}$$

such that $g_j(t, E)$ is able to reverse the effects of the structure on displacement $u_j(t, E)$, for some d.o.f. $1 \le j \le N$ and every $E \in I_E$. In Eq. (15), $\bar{\mathbf{X}}_l$, $\bar{W}_l(t)$ and $\bar{\mathcal{E}}_l(E)$ are space, time and parameter modes of the parametric IIR, which can be seen as the inverse of the parametric DIR, see Eq. (8). For simpler notation, we shall consider all d.o.f., that is $\mathbf{g}(t, E) \in \mathbb{R}^N$, but a subset of the d.o.f. could also be taken. Note that in particular, d.o.f. where essential boundary conditions apply should be excluded.

3.2.1 Randomized excitations and parametric optimization problem

As outlined in Section 3.1, to obtain the parametric IIR, a training set of forces and displacements must be known in advance, which can come from measurements or simulation. In our approach, we shall take advantage of the parametric DIR to generate a synthetic set of displacements inexpensively. In particular, we consider a set of n_{train} singleton excitations,

$$\mathcal{P} := \{p_\ell(t) : \; p_\ell(t) = \cos(\omega_\ell t), \; \omega_\ell \in I_\omega, \; 1 \le \ell \le n_{\text{train}}\}, \tag{16}$$

where ω_ℓ is drawn randomly from a uniform distribution. Thanks to the parametric DIR, $\mathbf{h}(t, E)$ defined in Section 2, we can compute the set of parametric displacements inexpensively by performing a convolution $\mathbf{h}(t, E) * p_\ell(t)$ for each element in $\mathcal{P}$. Specifically, at node j we have:

$$\mathcal{U} := \left\{ u_{\ell j}(t, E) : \; u_{\ell j}(t, E) = \sum_{i=1}^{n} X_{ij} \, \Upsilon_{i\ell}(t) \, \mathcal{E}_i(E), \; 1 \le \ell \le n_{\text{train}} \right\}, \tag{17}$$

where X_{ij} represents the j-th entry of $\mathbf{X}_i$ in Eq. (8). Observe that $u_{\ell j}(t, E)$ is written in separated-variables form, where $\Upsilon_{i\ell}(t) = W_i(t) * p_\ell(t)$. Recall that $W_i(t)$ is the i-th time-dependent mode of the parametric DIR.

Next, we proceed very much like in Eq. (12), i.e. we seek to minimize the mean square error between the estimate and the samples but this time including also the parameter domain:

$$\sum_{\ell=1}^{n_{\text{train}}} \|u_{\ell j}(t, E) * g_j(t, E) - p_\ell(t)\|^2 + \lambda \|S(g_j(t, E))\|^2, \tag{18}$$

where $\|\bullet\|$ denotes here the L^2 norm over $I_t \times I_E$ and $g_j(t, E)$ denotes the j-th entry of $\mathbf{g}(t, E)$. Again, note that each $g_j(t, E)$ in Eq. (18) can be computed independently from $g_k(t, E)$, with $k \neq j$.

By inserting parametric displacements definition given in Eq. (17) into Eq. (18), we arrive to the following parametric optimization problem: find $g_j(t, E)$, for $1 \leq j \leq N$, which is the minimizer of

$$\sum_{\ell=1}^{n_{\text{train}}} \left\| \left(\sum_{i=1}^{n} X_{ij} \Upsilon_{i\ell} \mathcal{E}_i \right) * g_j(t, E) - p_\ell(t) \right\|^2 + \lambda \|S(g_j(t, E))\|^2. \tag{19}$$

3.2.2 PGD method for parametric IIR computation

The stationarity condition of the functional Eq. (19) can be found by means of standard calculus of variations. Minimizing Eq. (19) is equivalent to solve the following problem: find $g_j \equiv g_j(t, E) \in L^2(I_t \times I_E)$ such that

$$\mathcal{A}(g_j, g_j^\star) + \lambda \mathcal{R}(g_j, g_j^\star) = \mathcal{L}(g_j^\star) \quad \forall g_j^\star \in L^2(I_t \times I_E), \tag{20}$$

where we have introduced the following bi-linear forms: $\mathcal{A}, \mathcal{R} : L^2(I_t \times I_E) \times L^2(I_t \times I_E) \to \mathbb{R}$ defined by

$$\mathcal{A}(u, u^\star) = \sum_{i,k=1}^{n} X_{ij} X_{kj} \int_{I_E} \int_{I_t} u^\star * (\mathcal{E}_i L_{ik} \mathcal{E}_k) * u \, dt \, dE,$$
$$\mathcal{R}(u, u^\star) = \int_{I_E} \int_{I_t} S(u^\star) S(u) \, dt \, dE, \tag{21}$$

as well as a linear form $\mathcal{L} : L^2(I_t \times I_E) \to \mathbb{R}$ defined by

$$\mathcal{L}(u^\star) = \sum_{i=1}^{n} X_{ij} \int_{I_E} \int_{I_t} u^\star * (q_i \mathcal{E}_i) \, dt \, dE. \tag{22}$$

Functions $L_{ik}(t)$ in Eq. (21) and $q_i(t)$ in Eq. (22) are defined as follows:

$$L_{ik}(t) = \sum_{\ell=1}^{n_{\text{train}}} \Upsilon_{i\ell}(t) \Upsilon_{k\ell}(t) \quad \text{and} \quad q_i(t) = \sum_{\ell=1}^{n_{\text{train}}} \Upsilon_{i\ell}(t) p_\ell(t). \tag{23}$$

In next lines we describe the PGD algorithm for the solution of Eq. (20). The main ingredients are a greedy algorithm for an incremental construction of the separated-variables representation and an alternating directions algorithm for the calculation of each separated-variables factor.

Greedy algorithm: PGD builds the separated-variables representation given of the solution, Eq. (15), by adding one term at a time. Therefore, assuming that $\bar{n}-1$ terms have already been computed, we seek a new term $\delta\mathbf{g}(t, E)$ such that the solution with $\bar{n}$ terms writes:

$$\mathbf{g}^{\bar{n}}(t, E) = \mathbf{g}^{\bar{n}-1}(t, E) + \delta\mathbf{g}(t, E) \tag{24}$$
$$\text{with} \quad \delta\mathbf{g}(t, E) = \bar{\mathbf{X}}\bar{W}(t)\bar{\mathcal{E}}(E).$$

Then, for a given d.o.f. $1 \leq j \leq N$, or a subset of them since they are uncoupled, the weak form given in Eq. (20) becomes: find $\delta g_j \in L^2(I_t \times I_E)$ such that

$$\mathcal{A}(\delta g_j, \delta g_j^\star) + \lambda\mathcal{R}(\delta g_j, \delta g_j^\star) = \mathcal{L}(\delta g_j^\star) - \mathcal{A}(g_j^{\bar{n}-1}, \delta g_j^\star) \tag{25}$$
$$\forall \delta g_j^\star \in L^2(I_t \times I_E).$$

The rank $\bar{n}$ can be adaptively chosen based on error estimates to achieve the desired precision [3, 26].

Alternating directions algorithm: Eq. (25) defines a nonlinear problem for the computation of the factors $\bar{\mathbf{X}}_j$, $\bar{W}(t)$ and $\bar{\mathcal{E}}(E)$ which is solved using an alternating directions linearization. These algorithms updates one factor at a time while considering the other factors fixed. The algorithm is stopped when it reaches a fixed point, i.e. the norm of the difference between two consecutive iterations is small enough. In next lines we derive the updates for each one of the factors:

- Update $\bar{\mathbf{X}}$. Assume both $\bar{W}$ and $\bar{\mathcal{E}}$ known from a previous iteration. Then, for $1 \leq j \leq N$ the test function becomes $\delta g_j^\star = \bar{X}_j^\star \bar{W}\bar{\mathcal{E}}$. After some tedious but conceptually simple manipulations, Eq. (25) becomes:

$$\alpha_X^j \bar{X}_j + \lambda\beta_X \bar{X}_j = \gamma_X^j - \eta_X^j. \tag{26}$$

  See Appendix A.1 for a detailed derivation. Coefficients α_X^j, β_X, γ_X^j and η_X^j are also given in the Appendix. In view of the above, $\bar{X}_j$ can be updated for every $1 \leq j \leq N$ by solving an uncoupled equation, i.e. a diagonal system because $\bar{X}_j$ does not depend on $\bar{X}_k$ for $k \neq j$:

$$\bar{X}_j = \frac{\gamma_X^j - \eta_X^j}{\alpha_X^j + \lambda\beta_X} \quad \Leftrightarrow \quad \bar{\mathbf{X}} = (\mathbf{D}_X + \lambda\beta_X\mathbf{I}_X)^{-1}(\boldsymbol{\gamma}_X - \boldsymbol{\eta}_X), \tag{27}$$

  where $\mathbf{D}_X$ is a diagonal matrix whose j-th diagonal entry is α_X^j, $\mathbf{I}_X$ is the identity in $\mathbb{R}^N$ and vectors $\boldsymbol{\gamma}_X$ and $\boldsymbol{\eta}_X$ collect γ_X^j and η_X^j, respectively, for $1 \leq j \leq N$.

- Update $\bar{W}$. Assume both $\bar{\mathbf{X}}$ and $\bar{\mathcal{E}}$ known from previous iterations. Then, for $1 \le j \le N$ the test function becomes $\delta g_j^{\star} = \bar{X}_j \bar{W}^{\star} \bar{\mathcal{E}}$. In this case, Eq. (25) becomes:

$$
\sum_{i,k=1}^{n} \alpha_T^{ik} \int_{I_t} \bar{W}^{\star} * L_{ik} * \bar{W} dt + \lambda \beta_T \int_{I_t} S(\bar{W}^{\star}) S(\bar{W}) dt =
$$
$$
= \sum_{i=1}^{n} \gamma_T^{i} \int_{I_t} \bar{W}^{\star} q_i dt - \sum_{i,k=1}^{n} \sum_{l=1}^{\bar{n}-1} \alpha_T^{ikl} \int_{I_t} \bar{W}^{\star} * L_{ik} * \bar{W}_l dt. \tag{28}
$$

See Appendix A.2 for a detailed derivation. Coefficients α_T^{ik}, β_T, γ_T^{i} and η_T^{ikl} are also given in the Appendix. After discretization of both time and Young modulus domains, we have:

$$
\bar{W} = \left(\mathbf{L}_T + \lambda \beta_T \mathbf{S}^T \mathbf{S} \right)^{-1} \left(\boldsymbol{\gamma}_T - \boldsymbol{\eta}_T \right), \tag{29}
$$

where $\mathbf{S}$ is the discrete counterpart of the linear operator $S(\bullet)$. Matrix $\mathbf{L}_T$ and vectors $\boldsymbol{\gamma}_T$ and $\boldsymbol{\eta}_T$ are given in the Appendix A.2.

- Update $\bar{\mathcal{E}}$. Assume both $\bar{\mathbf{X}}$ and $\bar{W}$ known from previous iterations. Then, for $1 \le j \le N$ the test function becomes $\delta g_j^{\star} = \bar{X}_j \bar{W} \bar{\mathcal{E}}^{\star}$. In this case, Eq. (25) becomes:

$$
\alpha_E \bar{\mathcal{E}} + \lambda \beta_E \bar{\mathcal{E}} = \gamma_E - \eta_E, \tag{30}
$$

See Appendix A.3 for a detailed derivation. Coefficients α_E, β_E, γ_E and η_E are also given in the Appendix. Observe that this is an uncoupled equation, i.e. for arbitrary $E_m \in I_E$, $\bar{\mathcal{E}}_m \equiv \bar{\mathcal{E}}(E_m)$ does not depend on $\bar{\mathcal{E}}_k$, with $m \ne k$. In view of the above, $\bar{\mathcal{E}}_m$ can be updated by solving an uncoupled equation, i.e. a diagonal system:

$$
\bar{\mathcal{E}}_m = \frac{\gamma_E^m - \eta_E^m}{\alpha_E^m + \lambda \beta_E} \quad \Leftrightarrow \quad \bar{\mathcal{E}} = (\mathbf{D}_E + \lambda \beta_E \mathbf{I}_E)^{-1} (\boldsymbol{\gamma}_E - \boldsymbol{\eta}_E), \tag{31}
$$

where $\alpha_E^m \equiv \alpha_E(E_m)$, and similarly for γ_E^m and η_E^m, with $1 \le m \le N_E$, being N_E the number of nodes used to discretize I_E. $\mathbf{D}_E$ is a diagonal matrix whose m-th diagonal entry is α_E^m, $\mathbf{I}_E$ is the identity matrix in $\mathbb{R}^{N_E}$ and vectors $\boldsymbol{\gamma}_E$ and $\boldsymbol{\eta}_E$ collect γ_E^m and η_E^m, respectively, for $1 \le m \le N_E$.

Remark (Avoiding regularization with the use of separated-variables representation). *Numerical evidence (see Section 4) shows that the PGD method can still be applied for solving Eq. (19) when no regularization is considered, i.e. $\lambda = 0$. PGD method shows stability in that case, and therefore it appears to have some kind of built-in regularization capabilities. A possible explanation may be related to the truncated Singular Values Decomposition as a regularization method, see [18]. This method expresses an approximated solution to*

the inverse problem by truncating the singular vectors associated to the smallest singular values (i.e. those related to high frequencies). A precise truncation can eliminate spurious oscillations introduced by the singular vectors associated to high frequencies. Because PGD proceeds in a greedy manner to minimize the mean square error, it first extracts the principal modes of the solution, which are indeed those associated to lower frequencies. Higher frequency spurious modes would only appear when PGD convergence is pushed to machine precision, which in practice is never done because we are usually in achieving effective model reduction. Research outside the scope of this paper would be needed to confirm this hypothesis.

4   Numerical example

In this section we describe the application of the method proposed in this paper to solve a numerical test case.

We consider 2D plate of size 1×1m and circular hole in the middle of radius 0.5m, as depicted in Fig. 2. The mesh contains 124 first-order triangular finite elements and 78 nodes. The plate is fixed at the bottom edge and a dynamic load is applied on the leftmost edge. Displacements are measured at the right upper corner of the plate (node P), which is marked in *red*. Homogeneous isotropic plane-stress visco-elasticity has been considered for the analysis, together with the Kelvin-Voigt model for the viscous part (see Section 2.1 for details). The mass density is considered $\rho = 1$kg/m^3, and the stiffness is considered as a parameter in a range of $E \in I_E = [10, 200]$Pa. The Kelvin-Voigt time constant, μ, is chosen such as to obtain make the damping factor $\xi = 10\%$. Recall that the ξ and μ are related via:

$$\xi = \frac{1}{2}\mu\omega_0 \quad \text{with} \quad \omega_0 = \sqrt{\sigma_0},$$

where σ_0 is the smallest eigenvalue (i.e. natural frequency) that results from solving the generalized eigenvalue problem $\mathbf{Ku} = \sigma\mathbf{Mu}$.

In the *offline* phase, both DIR and IIR are computed. For the computation of the DIR, a frequency is considered in a range $\omega \in I_\omega = [0, 500]$Hz, which allows for a time resolution of $\Delta t = 1$ms (recall Nyquist-Shannon theorem). The frequency domain is discretized using a step size $\Delta\omega = 10$mHz, which allows for a signal length $T_{\text{final}} = 1/2\Delta\omega = 100$s). Recall that frequency is a parameter of the parametric DIR. PGD algorithm converged after computing $n = 15$ modes. Fig. 3, Fig. 4 and Fig.5 show the space, frequency and Young modulus modes of the DIR, respectively. For the computation of the parametric IIR, a training set of $n_{\text{train}} = 10$ forces covering frequencies in a range of $[1, 25]$Hz has been considered. The PGD algorithm converged in this case after $\bar{n} = 80$ modes.

In order to validate the ability of the parametric IIR to recover the dynamic forces, we generate a set of synthetic displacement measures at node P. To this end, we consider three test forces with low, medium and high frequency spectrum, respectively. These forces were generated by fitting a cubic spline on

randomly drawn points. Therefore, none of this forces was explicitly contained in the training set used for computing the parametric IIR. The three test forces are shown in the leftmost column in Fig. 6. Notice that a shorter time scale has been chosen in these figures in order to distinguish high-frequency oscillations. The frequency spectrum of each test force is shown in the center column in Fig. 6. Then, structure displacements under the action of each test force can be computed using the parametric DIR. These are shown in the rightmost column in Fig. 6. It is worth to remark that these displacements are parametric, i.e. valid for all $E \in I_E$. However, in this numerical experiment we choose $E = 100\text{Pa}$, which only required a simple particularization of the parametric DIR. For clarity in the graphic representation, only displacements at measure node P are depicted.

Now, from the only knowledge of displacements *measured* at node P, we want to recover the dynamic forces (leftmost column in Fig. 6). To this end, we use the IIR previously computed, i.e. we apply Eq. (11) at node $j \equiv P$:

$$p_{\text{rec},i}(t) = \int_0^t u_{P,i}(t - \tau) \, g_P(\tau) \, d\tau, \quad i = 1, 2, \text{or } 3,$$

where $p_{\text{rec},i}(t)$ are the recovered test forces, $u_{P,i}(t)$ are displacements measured at node P and $g_P(t)$ is the inverse impulse response at node P. Observe that this equation only requires knowledge on the past signal, and therefore it respects causality. Furthermore, the computation to be made is so simple that real-time performance can be achieved effortlessly. Fig. 7 compares the three test forces that were recovered by the algorithm against the reference, showing a good matching. Relative errors, computed as in Eq. (32), were were $\varepsilon_1 = 3.5 10^{-6}$, $\varepsilon_2 = 6.3 10^{-7}$, $\varepsilon_3 = 8.1 10^{-7}$.

$$\varepsilon_i = \frac{\|p_{\text{rec},i}(t) - p_{\text{ref}}(t)\|}{\|p_{\text{ref}}(t)\|}. \tag{32}$$

5 Conclusions

In this paper, a methodology for real-time monitoring of both displacements and forces of linear time-invariant structures has been presented. Parametric solutions have been proven very useful in this context, as they have made possible: i) an enhanced version of the harmonic analysis; and ii) a comprehensive account for the system's variability via the solution's parametric nature. The PGD method was used to compute the parametric solutions with an efficient separated-variables representation, showing good computational performances in terms of both memory and execution time. Finally, we have proposed a strategy to compute the parametric solution of the inverse problem from the parametric solution of the direct problem. This approach, which is specifically designed for a parametric framework, makes use of synthetic samples generated from the solution of the direct problem. Most importantly, we have shown that the parametric domain does not need to be sampled to create the set of synthetic samples, which would in practice be unfeasible when several parameters

are considered. Hence, only the frequency domain needs to be sampled, making the computation of the parametric inverse solution very efficient.

A   Derivation of the update for PGD factors

In this section we give a detailed derivation of the equations for updating the PGD factors, as a part of the alternating directions algorithm presented in Section 3.2.2.

A.1   Updating the space factor $\bar{X}$

Both $\bar{W}$ and $\bar{\mathcal{E}}$ are assumed known from previous iterations. The test function reduces to $\delta g_j^\star = \bar{X}_j^\star \bar{W} \bar{\mathcal{E}}$. Then, the left-hand side of Eq. (25) becomes:

$$
\begin{aligned}
\mathcal{A}(\delta g_j, \delta g_j^\star) &= \sum_{i,k=1}^{n} \alpha_X^{ik} \bar{X}_j^\star X_{ij} X_{kj} \bar{X}_j \equiv \alpha_X^j \bar{X}_j^\star \bar{X}_j, \\
\mathcal{R}(\delta g_j, \delta g_j^\star) &= \beta_X \bar{X}_j^\star \bar{X}_j,
\end{aligned}
\tag{33}
$$

where we have introduced the coefficients α_X^{ik} and β_X defined below in Eq. (36). Coefficient α_X^j results from the contraction of the summations in Eq. (33). Likewise, the right-hand side of Eq. (25) becomes:

$$
\begin{aligned}
\mathcal{L}(\delta g_j^\star) &= \sum_{i=1}^{n} \gamma_X^i \bar{X}_j^\star X_{ij} \equiv \gamma_X^j \bar{X}_j^\star, \\
\mathcal{A}(g_j^{\bar{n}-1}, \delta g_j^\star) &= \sum_{i,k=1}^{n} \sum_{l=1}^{\bar{n}-1} \alpha_X^{ikl} \bar{X}_j^\star X_{ij} X_{kj} \bar{X}_{lj} \equiv \eta_X^j \bar{X}_j^\star,
\end{aligned}
\tag{34}
$$

where $\bar{X}_{lj}$ is the j-th component $\bar{\mathbf{X}}_l$, which is the l-th mode, $1 \leq l \leq \bar{n} - 1$, of $\mathbf{g}^{\bar{n}-1}(t, E)$, already known at this point of the computation; see Eq. (24). Coefficients γ_X^i and α_X^{ikl} are defined in Eq. (36). Coefficients γ_X^j and η_X^j result from the contraction of the summations in Eq. (34).

Considering Eq. (33) and Eq. (34) altogether, we arrive to:

$$
\alpha_X^j \bar{X}_j + \lambda \beta_X \bar{X}_j = \gamma_X^j - \eta_X^j.
\tag{35}
$$

The following coefficient definitions have been used in the above equations:

$$
\begin{aligned}
\alpha_X^{ik} &= \int_{I_E} \bar{\mathcal{E}} \mathcal{E}_i \mathcal{E}_k \bar{\mathcal{E}} \, dE \int_{I_t} \bar{W} * L_{ik} * \bar{W} \, dt, \\
\beta_X &= \int_{I_E} \bar{\mathcal{E}} \bar{\mathcal{E}} \, dE \int_{I_t} S(\bar{W}) S(\bar{W}) \, dt, \\
\gamma_X^i &= \int_{I_E} \bar{\mathcal{E}} \mathcal{E}_i \, dE \int_{I_t} \bar{W} * q_i \, dt, \\
\alpha_X^{ikl} &= \int_{I_E} \bar{\mathcal{E}} \mathcal{E}_i \mathcal{E}_k \bar{\mathcal{E}}_l \, dE \int_{I_t} \bar{W} * L_{ik} * \bar{W}_l \, dt.
\end{aligned}
\tag{36}
$$

A.2 Updating the time factor $\bar{W}$

Both $\bar{\mathbf{X}}$ and $\bar{\mathcal{E}}$ are assumed known from previous iterations. The test function reduces to $\delta g_j^\star = \bar{X}_j \bar{W}^\star \bar{\mathcal{E}}$. Then, the left-hand side of Eq. (25) becomes:

$$
\mathcal{A}(\delta g_j, \delta g_j^\star) = \sum_{i,k=1}^{n} \alpha_T^{ik} \int_{I_t} \bar{W}^\star * L_{ik} * \bar{W} dt,
$$

$$
\mathcal{R}(\delta g_j, \delta g_j^\star) = \beta_T \int_{I_t} S(\bar{W}^\star) S(\bar{W}) dt,
$$

(37)

where we have introduced the coefficients α_T^{ik} and β_T defined below in Eq. (39). Likewise, the right-hand side of Eq. (25) becomes:

$$
\mathcal{L}(\delta g_j^\star) = \sum_{i=1}^{n} \gamma_T^i \int_{I_t} \bar{W}^\star q_i dt,
$$

$$
\mathcal{A}(g_j^{\bar{n}-1}, \delta g_j^\star) = \sum_{i,k=1}^{n} \sum_{l=1}^{\bar{n}-1} \alpha_T^{ikl} \int_{I_t} \bar{W}^\star * L_{ik} * \bar{W}_l dt,
$$

(38)

where $\bar{W}_l$ is the l-th time-domain factor, $1 \leq l \leq \bar{n} - 1$, of $\mathbf{g}^{\bar{n}-1}(t, E)$, already known at this point of the computation; see Eq. (24). Coefficients γ_T^i and α_T^{ikl} are defined in Eq. (39).

The following coefficient definitions have been used in the above equations:

$$
\alpha_T^{ik} = \sum_{j=1}^{N} \bar{X}_j X_{ij} X_{kj} \bar{X}_j \int_{I_E} \bar{\mathcal{E}} \mathcal{E}_i \mathcal{E}_k \bar{\mathcal{E}} \, dE,
$$

$$
\beta_T = \sum_{j=1}^{N} \bar{X}_j \bar{X}_j \int_{I_E} \bar{\mathcal{E}} \bar{\mathcal{E}} \, dE,
$$

$$
\gamma_X^i = \sum_{j=1}^{N} \bar{X}_j X_{ij} \int_{I_E} \bar{\mathcal{E}} \mathcal{E}_i \, dE,
$$

$$
\alpha_X^{ikl} = \sum_{j=1}^{N} \bar{X}_j X_{ij} X_{kj} \bar{X}_{lj} \int_{I_E} \bar{\mathcal{E}} \mathcal{E}_i \mathcal{E}_k \bar{\mathcal{E}}_l \, dE.
$$

(39)

Finally, after discretization, the following definitions have been used in Eq. (29) (recall Eq. (23)):

$$
\mathbf{L}_T = \sum_{i,k=1}^{n} \alpha_T^{ik} \mathbf{L}_{ik} \equiv \sum_{i,k=1}^{n} \alpha_T^{ik} \sum_{\ell=1}^{n_{\text{train}}} \boldsymbol{\Upsilon}_{i\ell}^T \boldsymbol{\Upsilon}_{k\ell}
$$

$$
\boldsymbol{\gamma}_T = \sum_{i=1}^{n} \gamma_T^i \mathbf{q}_i \equiv \sum_{i=1}^{n} \gamma_T^i \sum_{\ell=1}^{n_{\text{train}}} \boldsymbol{\Upsilon}_{i\ell}^T \mathbf{p}_\ell
$$

$$
\boldsymbol{\eta}_T = \sum_{i,k=1}^{n} \sum_{l=1}^{\bar{n}-1} \alpha_T^{ikl} \mathbf{L}_{ik} \bar{\mathbf{W}}_l \equiv \sum_{i,k=1}^{n} \sum_{l=1}^{\bar{n}-1} \alpha_T^{ikl} \sum_{\ell=1}^{n_{\text{train}}} \boldsymbol{\Upsilon}_{i\ell}^T \boldsymbol{\Upsilon}_{k\ell} . \bar{\mathbf{W}}_l,
$$

(40)

where we have denoted by $\mathbf{\Upsilon}_{i\ell}$ (resp. $\mathbf{\Upsilon}_{k\ell}$) the discrete convolution operator associated to $\Upsilon_{i\ell}(t)$ (resp. $\Upsilon_{k\ell}(t)$).

A.3 Updating the parameter factor $\bar{\mathcal{E}}$

Both $\bar{\mathbf{X}}$ and $\bar{W}$ are assumed known from previous iterations. The test function reduces to $\delta g_j^\star = \bar{X}_j \bar{W} \bar{\mathcal{E}}^\star$. Then, the left-hand side of Eq. (25) becomes:

$$
\begin{aligned}
\mathcal{A}(\delta g_j, \delta g_j^\star) &= \sum_{i,k=1}^n \alpha_E^{ik} \int_{I_E} \bar{\mathcal{E}}^\star \mathcal{E}_i \mathcal{E}_k \bar{\mathcal{E}} dE, \\
\mathcal{R}(\delta g_j, \delta g_j^\star) &= \beta_E \int_{I_E} \bar{\mathcal{E}}^\star \bar{\mathcal{E}} dE,
\end{aligned}
\tag{41}
$$

where we have introduced the coefficients α_E^{ik} and β_E defined below in Eq. (45). Likewise, the right-hand side of Eq. (25) becomes:

$$
\begin{aligned}
\mathcal{L}(\delta g_j^\star) &= \sum_{i=1}^n \gamma_E^i \int_{I_E} \bar{\mathcal{E}}^\star \mathcal{E}_i dE, \\
\mathcal{A}(g_j^{\bar{n}-1}, \delta g_j^\star) &= \sum_{i,k=1}^n \sum_{l=1}^{\bar{n}-1} \alpha_E^{ikl} \int_{I_E} \bar{\mathcal{E}}^\star \mathcal{E}_i \mathcal{E}_k \bar{\mathcal{E}}_l dE,
\end{aligned}
\tag{42}
$$

where $\bar{\mathcal{E}}_l$ is the l-th parameter factor, $1 \le l \le \bar{n} - 1$, of $\mathbf{g}^{\bar{n}-1}(t, E)$, already known at this point of the computation; see Eq. (24). Coefficients γ_E^i and α_E^{ikl} are defined in Eq. (45).

Note that, very much like in Section A.1, the computation of $\bar{\mathcal{E}}$ is algebraic, i.e. for arbitrary $E_m \in I_E$, the solution $\bar{\mathcal{E}}_m \equiv \bar{\mathcal{E}}(E_m)$ is uncoupled with respect to all $\bar{\mathcal{E}}_k$ for $k \ne m$. Therefore, let us write both Eq. (41) and Eq. (42) into their strong form:

$$
\sum_{i,k=1}^n \alpha_E^{ik} \mathcal{E}_i \mathcal{E}_k \bar{\mathcal{E}} + \lambda \beta_E \bar{\mathcal{E}} = \sum_{i=1}^n \gamma_E^i \mathcal{E}_i - \sum_{i,k=1}^n \sum_{l=1}^{\bar{n}-1} \alpha_E^{ikl} \mathcal{E}_i \mathcal{E}_k \bar{\mathcal{E}}_l,
\tag{43}
$$

which reduces to:

$$
\alpha_E \bar{\mathcal{E}} + \lambda \beta_E \bar{\mathcal{E}} = \gamma_E - \eta_E,
\tag{44}
$$

upon contraction of the summations, defining coefficients α_E, β_E, γ_E and η_E.

The following coefficient definitions have been used in the above equations:

$$
\begin{aligned}
\alpha_E^{ik} &= \sum_{j=1}^{N} \bar{X}_j X_{ij} X_{kj} \bar{X}_j \int_{I_t} \bar{W} * L_{ik} * \bar{W} \, dt, \\
\beta_E &= \sum_{j=1}^{N} \bar{X}_j \bar{X}_j \int_{I_t} S(\bar{W}) S(\bar{W}) \, dt, \\
\gamma_E^i &= \sum_{j=1}^{N} \bar{X}_j X_{ij} \int_{I_t} \bar{W} * q_i \, dt, \\
\alpha_E^{ikl} &= \sum_{j=1}^{N} \bar{X}_j X_{ij} X_{kj} \bar{X}_{lj} \int_{I_t} \bar{W} * L_{ik} * \bar{W}_l \, dt.
\end{aligned}
\tag{45}
$$

References

[1] Abbiati, G., Bursi, O. S., Caperan, P., Di Sarno, L., Molina, F. J., Paolacci, F., and Pegon, P. (2015) *Hybrid simulation of a multi-span RC viaduct with plain bars and sliding bearings.* Earthquake Engng Struct. Dyn., 44: 2221-2240.

[2] Aguado J.V., Huerta A., Chinesta F., Cueto E. *Real time monitoring of thermal processes by reduced order modeling.* International Journal for Numerical Methods in Engineering, 102 (5), 991-1017, 2015.

[3] Ammar, A., Chinesta, F., Díez, P., and Huerta, A. (2010a). An error estimator for separated representations of highly multidimensional models. Comput. Meth. Appl. Mech. Engrg., 199(25-28):1872–1880.

[4] Bathe, K.-J. (2006). Finite Element Procedures. Civil engineering series. Prentice-Hall, Englewood Cliffs, NJ.

[5] Belytschko, T., Fish, J.. *A First Course in Finite Elements.* 2007. 0470035803. John Wiley and Sons, Inc. USA

[6] Bertero, M., Bocacci, P., *introduction to inverse problems in imaging*, 1998, CRC Press.

[7] Bleyer, I. R., Leitão, A.. Novel regularization methods for ill-posed problems in Hilbert and Banach spaces, 2015, Brazil: Publicações matemáticas do IMPA. 121 p. (30 Colóquio Brasileiro de Matemática).

[8] Bialecki, R., Kassab, A., and Fic, A. *Proper Orthogonal Decomposition and Modal Analysis for acceleration of transient FEM thermal analysis.* Int. J. Numer. Meth. Engng., 62(6):774-797. 2005.

[9] Chinesta, F., Ladevèze, P., and Cueto, E. *A short review on model order reduction based on Proper Generalized Decomposition.* Arch. Comput. Methods Eng., 18(4):395-404. 2011.

[10] Chinesta F, Leygue A, Bordeu F, Aguado J, Cueto E, Gonzalez D, Alfaro I, Ammar A, Huerta A. *PGD-based computational vademecum for efficient design, optimization and control*. Archives of Computational Methods in Engineering. 20(1):31-59. 2013.

[11] Clough R.W., Penzien J. *Dynamics of Structures*. 2nd edition. McGraw-Hill. New York, 1993.

[12] Roy R. Craig, Andrew J. Kurdila. Fundamentals of Structural Dynamics, 2nd Edition. ISBN: 978-0-471-43044-5. Jul 2006. 744 pages

[13] Duriez. Y, Coevoet, E., Largilliere, F., Bieze T., Zhang Z., et al.. *Framework for online simulation of soft robots with optimization-based inverse model*. SIMPAR: IEEE International Conference on Simulation, Modeling, and Programming for Autonomous Robots, Dec 2016, San Francisco, United States. 2016, Proceedings of SIMPAR 2016 conference.

[14] Gonzalez, D., Cueto, E., and Chinesta, F. (2014). Real-time direct integration of reduced solid dynamics equations. *Int. J. Numer. Meth. Engng.*, 99(9):633–653.

[15] Gonzalez, D., Alfaro, I., Quesada, C., Cueto, E., and Chinesta, F. (2015). Computational Vademecums for the real-time simulation of haptic collision between nonlinear solids. textitComput. Meth. Appl. Mech. Engrg., 283:210–22.

[16] Einicke, G.A.; White, L.B. (September 1999). "Robust Extended Kalman Filtering". IEEE Trans. Signal Processing. 47 (9): 2596-2599.

[17] Germoso, Claudia, Aguado, Jose V., Fraile, Alberto, Alarcon, Enrique, Chinesta, Francisco. (2015). Efficient PGD-based dynamic calculation of non-linear soil behavior. Comptes Rendus Mécanique. 344. 10.1016/j.crme.2015.09.002.

[18] Hansen, P.C. Deconvolution and Regularization with Toeplitz Matrices. Numerical Algorithms (2002) 29:323.

[19] Hansen, P.C. *Rank-Deficient and Discrete Ill-Posed Problems*. SIAM, Philadelphia, PA, 1998.

[20] Hetmaniuk, U., Tezaur, R., and Farhat, C. (2012). Review and assessment of interpolatory model order reduction methods for frequency response structural dynamics and acoustics problems. *Int. J. Numer. Meth. Engng.*, 90(13):1636–1662.

[21] Hughes, T. J. R. (2000). The finite element method: linear static and dynamic finite element analysis. Dover Publications, New York. Corrected reprint of the 1987 original, Prentice Hall, Englewood Cliffs, NJ.
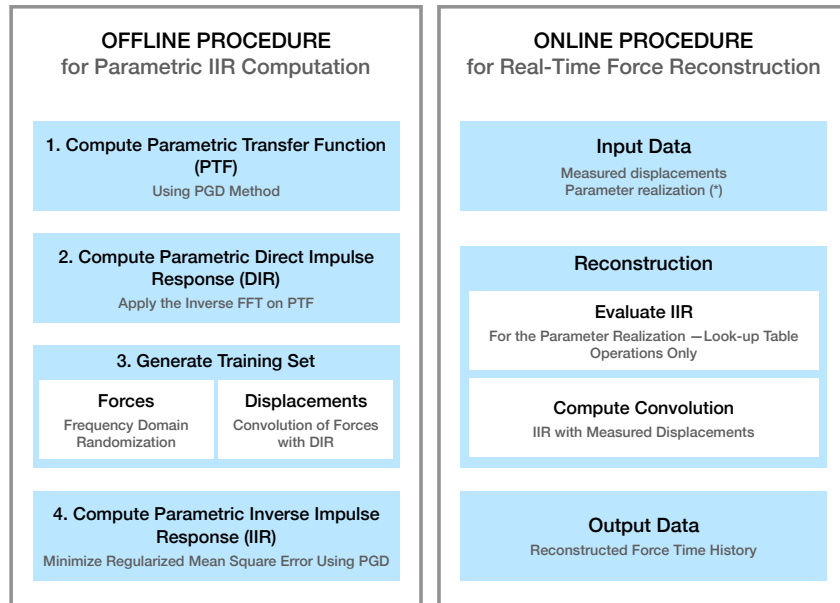
[22] Jérôme Idier. Bayesian Approach to Inverse Problems. ISTE Ltd and John Wiley and Sons Inc, pp.384, 2008. hal-00400668

[23] Z Jiang, SJ Kim, S Plude, R Christenson. Real-time hybrid simulation of a complex bridge model with MR dampers using the convolution integral method. Smart Materials and Structures. 22 105008. 2013.

[24] R. E. Kalman, "A new approach to linear filtering and prediction problems," Journal of Fluids Engineering, vol. 82, no. 1, pp. 35-45,1960

[25] Kochukhov O., Makaganiuk V., Piskunov N. *Least-Squares deconvolution of the stellar intensity and polarization spectra.* Astron. Astrophys.524, A.5.

[26] Lavedèze, P. and Chamoin, L. (2011). On the verification of model reduction methods based on the Proper Generalized Decomposition. Comput. Meth. Appl. Mech. Engrg., 200(23-24):2032–2047.

[27] Landweber, L. *An iteration formula for Fredholm integral equations of the first kind.* Amer. J. Math. 73, 615–624, 1951.

[28] Malik Muhammad Haris, Domenico Borzacchiello, José Vicente Aguado, Francisco Chinesta. Advanced parametric space-frequency separated representations in structural dynamics: A harmonic-modal hybrid approach. Comptes Rendus Mécanique, Elsevier Masson, 2018, 346(7), pp.590-602.

[29] Maday, Y., Patera, A., and Turinici, G. *A priori convergence theory for reduced-basis approximations of single-parametric elliptic partial differential equations.* J. Sci. Comput., 17(1-4):437-446. 2002.

[30] Proakis JG, Manolakis DG, *Digital Signal Processing*, 4th edition, Prentice Hall, ISBN, Sec 2. 2002

[31] Rouch, P. and Blanzé, C. (2014). Vibrational analysis of structures with stochastic interfaces in the medium-frequency range: Experimental validation on a touch screen. *J. Sound Vibr.*, 333(6):1612-1628.

[32] Rouch, P. and Ladeveèze, P. (2003). The Variational Theory of Complex Rays: A predictive tool for medium-frequency vibrations. *Comput. Meth. Appl. Mech. Engrg.*, 192(28-30):3301-3315.

[33] D. Rus and M. T. Tolley, *Design, fabrication and control of soft robots* Nature, vol. 521, no. 7553, 2015

[34] Silvia. M., Robinson, E. *Deconvolution of Geophysical Time Series in the Exploration for Oil And Natural Gas*, V. 10. 1st Edition. 1979. Elsevier.

[35] Tikhonov AN, Arsenin VY. *Solutions of ill-posed problems* Wiley. New York. 1997.

[36] Tisseur, F. and Meerbergen, K.. *The Quadratic Eigenvalue Problem.* SIAM Rev., 43(2):235-286. 2001.

[37] Zanella R., Zanghirati G., Cavicchioli R., Zanni L., Boccacci P., Bertero M., Vicidomini G. *Towards real-time image deconvolution: application to confocal and STED microscopy*. Scientific Reports 3 2523, 2013.

[38] Zienkiewicz OC, Taylor RL. *The Finite Element Method*. Vol. 2 Solid Mechanics (5th edn). Butterworth Heinemann: Oxford, 2000.

[39] Zu-Qing Qu. *Model Order Reduction Techniques with Applications in Finite Element Analysis*. Springer, London. 2004, 978-1-4471-3827-3.

[40] FJ Herrada, J García-Martínez, A Fraile, LKH Hermanns, FJ Montáns. *A method for performing efficient parametric dynamic analyses in large finite element models undergoing structural modifications*. Engineering Structures 131, 625-638.

[41] J. García-Martínez, F.J. Herrada, L.K.H. Hermanns, A. Fraile, F.J. Montáns. *Accelerating parametric studies in computational dynamics: Selective modal re-orthogonalization versus model order reduction methods*. Advances in Engineering Software 2017. 108:24-36.

[42] E. Jacquelin, A. Bennani, P. Hamelin. *Force reconstruction: analysis and regularization of a deconvolution problem*. Journal of Sound and Vibration 2003. 265:81-107.

[43] M. Klinkov, C.P. Fritzen. *An updated comparison of the force reconstruction methods*. Key Engineering Materials 2007. 347:461-466.

[44] S. Guillijns, B. De Moor. *Unbiased minimum-variance input and state estimation for linear discrete-time systems with direct feedthrough*. Automatica 2007. 43:934-937.

[45] J. Sanchez, H. Benaroya. *Review of force reconstruction techniques*. Journal of Sound and Vibration 2014. 333:2999-3018.

[46] E. Lourens, E. Reynders, G. De Roeck, G. Degrande, G. Lombaert. *An augmented Kalman filter for force identification in structural dynamics*. Mechanical Systems and Signal Processing 2012. 27:446-460.

[47] E. Lourens, C. Papadimitriou, S. Guillijns, E. Reynders, G. De Roeck, G. Lombaert. *Joint input-response estimation for estructural systems based on reduced-order models and vibration data from a limited number of sensors*. Mechanical Systems and Signal Processing 2012. 29:310-327.

[48] D. Bernal, A. Ussia. *Sequential deconvolution input reconstruction*. Mechanical Systems and Signal Processing 2015. 50-51:41-55.

[49] K. Maes, A.W. Smyth, G. De Roeck, G. Lombaert. *Joint input-state estimation in structural dynamics*. Mechanical Systems and Signal Processing 2016. 70-71:445-466.

[50] Bellman, R.E. *Dynamic Programming*. Courier Dover Publications, New York, republished edition, 2003.

[51] Kolda, T. and Bader, B. *Tensor decompositions and applications*. SIAM Rev. 2009. 51(3):455–500.

[52] Hasanov, A., Baysal, O. and Sebu, C. *Identification of an unknown shear force in the Euler-Bernoulli cantilever beam from measured boundary deflection*. Inverse Probl. 2019. In press, doi:10.1088/1361-6420/ab2a34.

Alemdar Hasanov1, onur baysal2 and Cristiana Sebu3

List of Figures

OFFLINE PROCEDURE
for Parametric IIR Computation

1. Compute Parametric Transfer Function (PTF)
Using PGD Method

2. Compute Parametric Direct Impulse Response (DIR)
Apply the Inverse FFT on PTF

3. Generate Training Set

Forces	Displacements
Frequency Domain Randomization	Convolution of Forces with DIR

4. Compute Parametric Inverse Impulse Response (IIR)
Minimize Regularized Mean Square Error Using PGD

ONLINE PROCEDURE
for Real-Time Force Reconstruction

Input Data
Measured displacements
Parameter realization (*)

Reconstruction

Evaluate IIR
For the Parameter Realization —Look-up Table Operations Only

Compute Convolution
IIR with Measured Displacements

Output Data
Reconstructed Force Time History

(*) Accounts for structural alterations or uncertainties. Depending on the application, it can be measured, assumed or simply guessed, as a part of an inverse identification algorithm for instance.

Figure 1: General picture of the method.
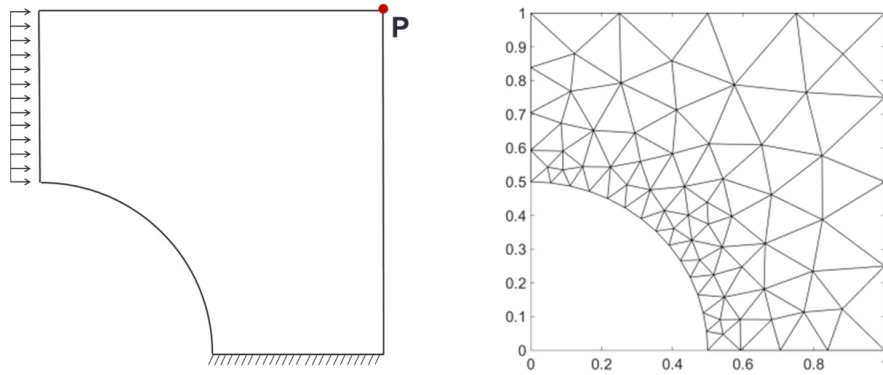
Figure 2: Geometry and mesh of the numerical test case: a 2D plate with of size 1×1m and circular hole in the middle of radius 0.5m. Measure node P is marked in red.
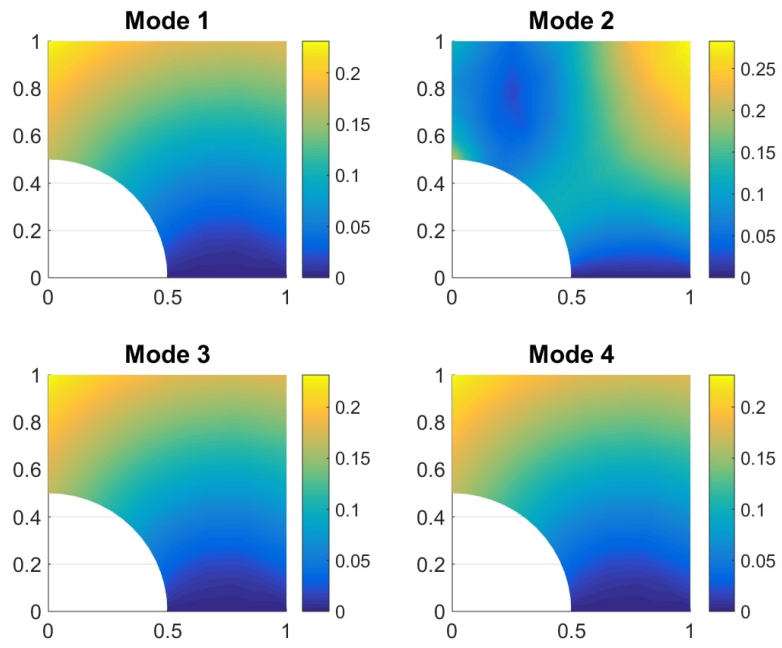
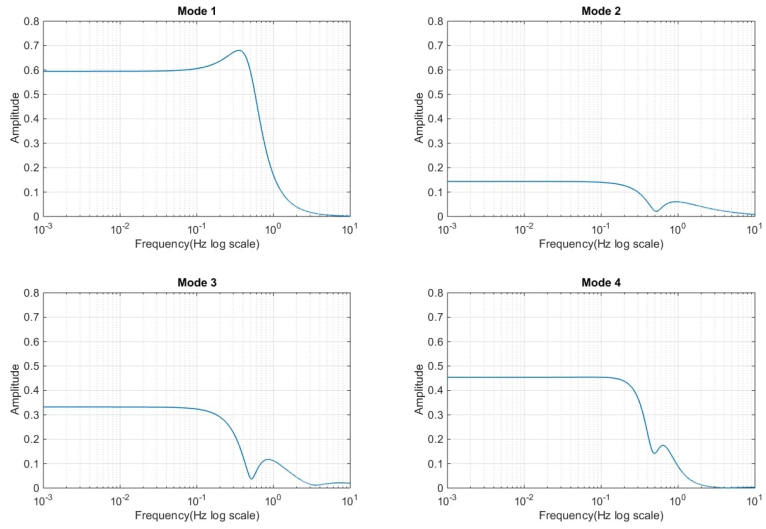Figure 3: First four space modes of the parametric direct impulse response.

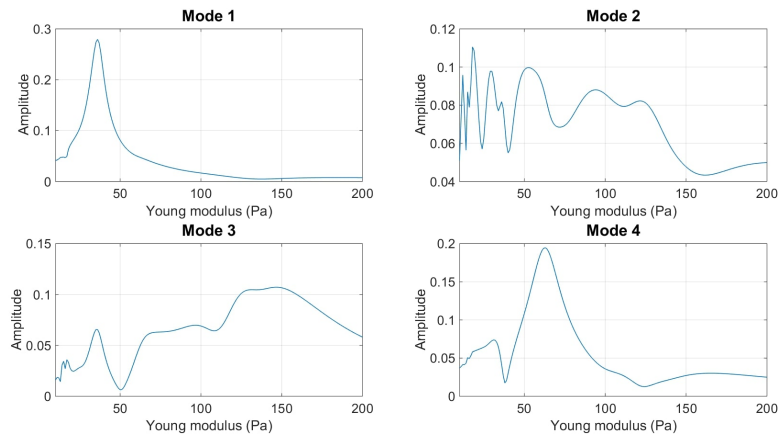Figure 4: First four frequency modes of the parametric direct impulse response.

Figure 5: First four Young's modulus modes of the parametric direct impulse response.
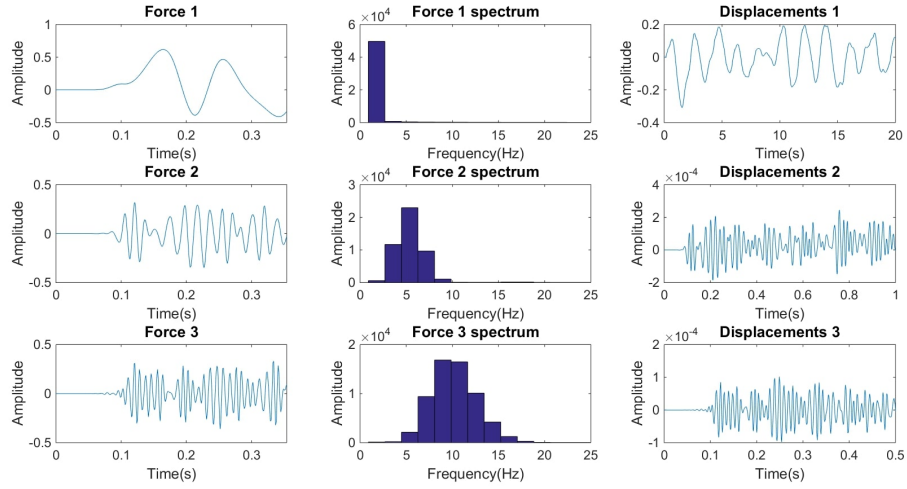
Figure 6: Test forces and synthetic displacements at measure node P for validation. Left column: three test forces with low, medium and high frequency content. Center column: frequency spectra of the test forces. Right column: displacements at point P under the action of the test forces.
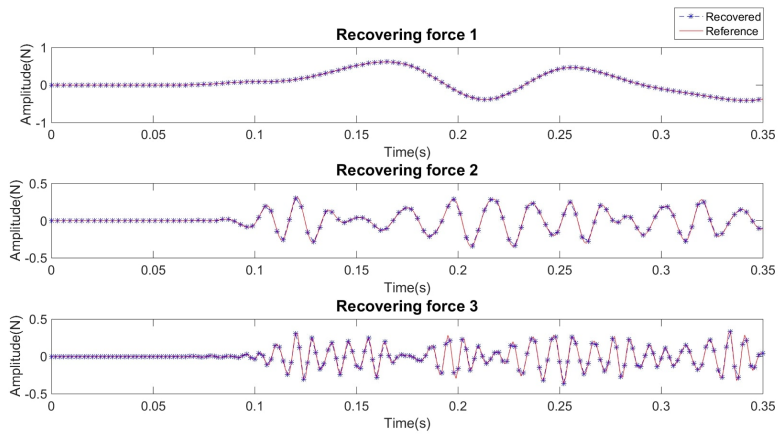
Figure 7: Comparison of the recovered dynamic forces against the reference shows good agreement.